



HAL
open science

Single LiBH₄ nanocrystal stochastic impacts at a micro water|ionic liquid interface

Jane Talia Stockmann, Jean-François Lemineur, Huiyin Liu, Claudio Cometto, Marc Robert, Catherine Combellas, Frédéric Kanoufi

► **To cite this version:**

Jane Talia Stockmann, Jean-François Lemineur, Huiyin Liu, Claudio Cometto, Marc Robert, et al.. Single LiBH₄ nanocrystal stochastic impacts at a micro water|ionic liquid interface. *Electrochimica Acta*, 2018. hal-01974517

HAL Id: hal-01974517

<https://u-paris.hal.science/hal-01974517>

Submitted on 8 Jan 2019

HAL is a multi-disciplinary open access archive for the deposit and dissemination of scientific research documents, whether they are published or not. The documents may come from teaching and research institutions in France or abroad, or from public or private research centers.

L'archive ouverte pluridisciplinaire **HAL**, est destinée au dépôt et à la diffusion de documents scientifiques de niveau recherche, publiés ou non, émanant des établissements d'enseignement et de recherche français ou étrangers, des laboratoires publics ou privés.

Single LiBH₄ nanocrystal stochastic impacts at a micro water|ionic liquid interface

T. Jane Stockmann,^{a,b,*} Jean-François Lemineur,^b Huiyin Liu,^b Claudio Cometto,^c Marc Robert,^c Catherine Combellas,^b and Frédéric Kanoufi^{b,*}

^a*Memorial University of Newfoundland, Department of Chemistry, St. John's NL Canada, A1B 3X7*

^b*Sorbonne Paris Cité, Paris Diderot University, Interfaces, Traitements, Organisation et Dynamique des Systèmes, CNRS-UMR 7086 15 rue J. A. Baïf, 75013 Paris (France)*

^c*Sorbonne Paris Cité, Laboratoire d'Electrochimie Moléculaire, UMR 7591 Université Paris Diderot - CNRS, 15 rue J.A. de Baïf, 75013 Paris (France)*

Corresponding Authors: T. Jane Stockmann, tstockmann@mun.ca; Frédéric Kanoufi, frederic.kanoufi@univ-paris-diderot.fr

Abstract. LiBH₄ is often employed as a reducing agent for metal nanoparticle (NP) preparation but is inherently a solid-state H₂ hydrogen storage agent. Herein it is shown, through a combination of electron/optical microscopies and single entity electrochemical study, that LiBH₄ is stored in the solid state within an ionic liquid (IL) as nanocrystals (NCs). The electrochemical monitoring of an immiscible water|IL (w|IL) micro-liquid|liquid interface (LLI) shows interfacial charge exchange associated with the stochastic impacts of single NCs. Meanwhile, *in situ* optical monitoring of a w|metal or w|IL interface shows that such impacts are associated with the development of a H₂-in-IL micro/nano-foam related to the poor solubility of H₂. Both the presence of solid NCs and the latter H₂-in-IL foam suggest that H₂ release from LiBH₄-in-IL is a slow, but likely controlled process. The rate of H₂ production at a macroscopic LLI is further confirmed by gas chromatographic measurements, in very good agreement with microscopic observations. The electrochemical LLI provides unique investigative access to LiBH₄ NCs and offers insight into H₂ storage in ILs, or for direct borohydride fuel cells, as well as NP synthesis.

Highlights:

1. Single entity electrochemical detection of LiBH_4 nanocrystals at a water|ionic liquid interface.
2. Single H_2 bubble generated from LiBH_4 nanocrystals inside an ionic liquid.
3. LiBH_4 induced H_2 -in-ionic liquid foam at water|ionic liquid interface.

Keywords (5):

LiBH_4 nanocrystals, ionic liquid, nano-impacts, liquid|liquid, H_2 storage

1.0 Introduction

Lithium borohydride (LiBH_4) and its analogues have been proposed for a variety of energy and synthetic applications, including H_2 storage [1-4], direct borohydride fuel cells [5, 6], and as reducing agents – both molecular and in the formation of metal nanoparticles (NPs) [4, 7]. Simultaneously, ionic liquids (ILs) have been used as industrial solvents for chemical processes, where the environmental impact has been reduced relative to molecular solvents, the reactivity enhanced, and with better recovery of catalytic materials [8]. However, the dissolution or suspension of inorganic salts within the IL phase is rarely discussed [9]. These materials, either added intentionally or present as impurities, will likely influence IL solvent effectiveness or introduce new reactivity. Interestingly, for the specific case of metal-NP synthesis within an IL the supramolecular nature of the IL produces highly monodisperse particles with sizes ranging as low as 1-2nm [7, 10-15] when LiBH_4 is used as a reducing agent. In most of these synthetic applications, and for the case of H_2 storage, an excess of borohydride is required. It has been demonstrated, however, that adventitious borohydride and borate species can behave as Lewis acid catalysts themselves [14, 16, 17]. Indeed, Banerjee *et al.* [14] showed both borohydride and borate provided efficient dehydrogenation of cyclohexanol within an IL.

However, these studies often minimize the contribution of LiBH_4 solubility in the ILs, which may be detrimental or beneficial, but should definitely be controlled for improved understanding of such reactive systems (NP synthesis, catalysis, H_2 storage, *etc.*). If IL systems are to be used in, for example, industrial electrocatalysis, the activity of possible residual material from different preparation methods needs to be resolved. For the case of LiBH_4 , its insolubility would likely lead to poor mass transport of suspended LiBH_4 crystals, and therefore, limited access to H_2 for chemical storage capabilities. Herein, we were able to grow LiBH_4 nanocrystals (NCs) within two quaternized phosphonium salts: trihexyltetradecylphosphonium bis(trifluoromethylsulfonyl)imide ($\text{P}_{66614}\text{NTf}_2$) and tetraoctylphosphonium bromide (P_{8888}Br). The former is an IL, while the latter is an organic ionic plastic crystal (OIPC), *i.e.* is plastic at room temperature [18]. This IL and OIPC were chosen for several reasons. First, both are hydrophobic and likely to have poor solubility towards polar inorganic salts such as LiBH_4 . Next, we have developed synthetic protocols to generate both in high purity at relatively low cost. Finally, the physicochemical characteristics of $\text{P}_{66614}\text{NTf}_2$ are well known and thus it can be employed as a model system.

To test the reactivity of LiBH_4 NCs, single entity stochastic impacts at the water| $\text{P}_{66614}\text{NTf}_2$ (w| $\text{P}_{66614}\text{NTf}_2$) micro-interface were employed. Single NP or nano-object studies

have emerged as a critical tool to investigate nanoscale charge transfer processes [19, 20]. Through Brownian motion, NPs collide with a polarized interface, either a solid/solution [21-29] or a liquid|liquid interface (LLI) [30-34], and are detected electrochemically through either oxidation/reduction of the NP itself, or via electron transfer through the NP, which enhances electrocatalytically a heterogeneous reaction at its surface [19, 20]. Heyrovsky *et al.* pioneered the field of soft LLI ensemble measurements with SnO₂, TiO₂, and Fe₂O₃ colloid adsorption at a Hg electrode [35-38]. Later, Bard's [24, 39, 40] and Compton's [27, 41] groups examined attolitre foam impacts at solid ultramicroelectrodes. Our group then transposed electrochemical single metal NP detection to the micro water|oil (w|o) immiscible LLI.[31] Herein, we expand this technique to the w|IL one, where the Galvani potential difference across the interface, $\phi_w - \phi_{IL} = \Delta_{IL}^w \phi$, is controlled by electrodes immersed in either phase, allowing control and quantification of charge transfer across the LLI. Transmission electron microscopy (TEM) and stochastic impacts were used to provide NC sizing, while optical microscopies (back absorbing layer, BALM [42, 43], and darkfield [28, 44-46]) provided *in situ* visualisation of the reactivity of such NCs in solution. The latter have emerged as powerful techniques for imaging objects *in situ* below the diffraction limit of classical bright-field optical microscopies (<500nm) and have been used effectively for NP sizing as well as for monitoring the transport, electrochemical transformation or growth of NPs at nano/microelectrodes or pipettes [28, 42, 47-51]. Besides monitoring of catalytic product formation, Tao also demonstrated the ability of SPR-based optical microscopy to monitor H₂ production by individual Pt NPs [52]. Herein optical images at a w|IL LLI held at the tip of a pulled pipette were used to evidence *in situ* the formation of micrometric H₂ bubbles associated with interfacial nanocrystal transformation in the IL. The ensemble of all these microscopic inspections bridge the gap between single entity optical or electrochemical study and the macroscopic gas evolution propensity of P₆₆₆₁₄NTf₂ LiBH₄ solutions or P₈₈₈₈Br OIPCs for H₂ evolution (or H₂ storage) that is evaluated herein by gas chromatography (GC).

2.0 Experimental Section

2.1 Materials

All chemicals were used as received unless otherwise stated. Li₂SO₄ (>99%), H₂SO₄ (>95%), trihexyltetradecylphosphonium bromide (P₆₆₆₁₄Br, >95%), lithium bis(trifluoromethylsulfonyl)imide (LiNTf₂, >99%), trioctylphosphine (97%), 1-bromooctane (99%), 2.0M LiBH₄ in THF, and CH₂Cl₂ (>99%) were purchased from Sigma-Aldrich. P₆₆₆₁₄NTf₂ was prepared by metathesis of P₆₆₆₁₄Br and LiNTf₂ in CH₂Cl₂; the resultant IL was washed several times with

water. Tetraoctylphosphonium bromide ($P_{8888}Br$) was prepared as detailed elsewhere through reaction of trioctylphosphine and 1-bromooctane [18]. During the preparation of tetraalkylphosphonium halides, side reactions often produce the acid halide and acid salt (*e.g.* trihexyltetradecylphosphonium hydrochloride) as impurities as described by Bradaric *et al.* [53]. For the case of $P_{66614}NTf_2$, additional impurities include residual LiBr. However, both were colourless and transparent indicating very low levels of impurities. All aqueous solutions were prepared using Milli-Q water ($>18.2M\Omega$ cm).

IL- $LiBH_4$ solutions were prepared by injecting 1.5mL of 2.0M $LiBH_4$ in THF into a two-neck round-bottom flask containing 5g of $P_{66614}NTf_2$ or $P_{8888}Br$ under Ar at 60°C. THF was removed at 80°C under high vacuum overnight.

2.2 Electrochemistry

All electrochemical measurements were performed in a grounded Faraday cage using a CH instruments (model#660, Austin TX) potentiostat with a minimum sample interval of 0.008s or 125Hz in the chronoamperometric mode. The electrolytic cell consisted of a pulled borosilicate capillary with a micro-interface (25 μ m in diameter) inserted into a holder equipped with Pt electrode, connected to the working electrode lead of the potentiostat, and a syringe. The latter maintained the LLI at the tip of the pipette when submerged in a vial containing the IL phase and another Pt electrode connected to the counter and reference leads. Micro-pipette fabrication and specifications are described elsewhere [54, 55]. In this way, Cell 1 can be described by the following:



where x is the final $LiBH_4$ concentration after THF evaporation.

2.3 Instrumentation

Transmission electron microscopy (TEM) images were acquired using a JEM 2010 (JEOL Company). Particle sizing was performed using the ImageJ software and samples were deposited on to a lacey carbon 200 mesh copper grid.

Dynamic light scattering (DLS) measurements were performed with the Malvern Zetasizer Nano ZS90 using a micro volume quartz cuvette. All data were reported from % intensity plots.

Backside absorbing layer microscopy observations were achieved on a Zeiss Axiovert.A1 inverted microscope. The polychromatic and unpolarized light was generated by an LED and the

antireflective sample was illuminated from the glass side. The contrast layer was purchased from WatchLive SAS and consisted of an ultrathin film of gold deposited on a glass slide. The thickness of the gold layer was chosen to be roughly 5nm to approach the anti-reflection conditions. The reflected light was collected through a 63× oil immersion objective with a numerical aperture of 1.40 and was captured with an IDS 8 bits CMOS camera. IL samples were deposited on the BALM substrate with the help of a micropipette and were imaged under atmospheric conditions.

Darkfield optical microscopy was carried out with an Olympus IX71 inverted microscope equipped with a Sony XCD-X710 CCD camera and darkfield condenser along with 10×, 40×, and 60× objectives, NA = 0.3, 0.60, and 0.70, respectively, as described in detail elsewhere [44].

Gas Chromatography (GC) analysis from gas evolved into the headspace of a vial (sealed with a cap incorporating a septum, total volume ~1.8mL) during reaction was performed with an Agilent Technologies 7820A GC system equipped with a thermal conductivity detector. H₂ production was quantitatively assessed using a CP-CarboPlot P7 capillary column (27.46m in length and 25μm internal diameter). Temperature was held at 150°C for the detector and 34°C for the oven. An argon carrier gas flowing at 9.5mL min⁻¹ at constant pressure of 0.5bar was employed, while injection was performed via a 250-μL gas-tight (Hamilton) syringe. These conditions allowed for separation of H₂, O₂, and N₂. Calibration curves for H₂ were determined separately by injecting known quantities of pure gas.

3.0 Results and Discussion

In a typical metal NP-in-IL synthesis, LiBH₄, dissolved in tetrahydrofuran (THF), is injected into an IL solution, containing a transition metal salt, under an inert atmosphere [13, 14]. THF is then removed under high vacuum at 80°C. In order to investigate the role of LiBH₄, no transition metal salt (e.g. KAuCl₄ or PtCl₂) was added. Fig. 1A depicts a cyclic voltammogram (CV) obtained using Cell 1 (see Experimental Section and Fig. S1 of the Supplementary Information, SI) at a w|P₆₆₆₁₄NTf₂ LLI with 5mM of Li₂SO₄ (aq), but without LiBH₄ added to the IL (a blank curve); a scan rate of 0.02V s⁻¹ was used unless otherwise noted.

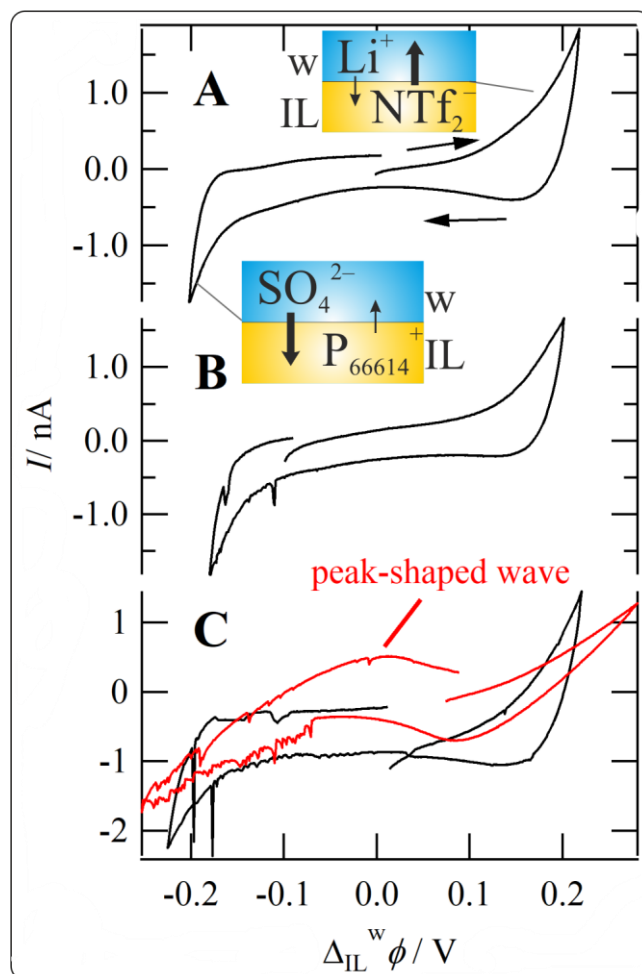


Figure 1: Cyclic voltammograms at a w|P₆₆₆₁₄NTf₂ LLI using Cell 1 (Exp. Sect.) with 5mM Li₂SO₄ (aq) and 0, 20, and 600mM [LiBH₄] for curves A, B, and C, respectively. The potential is referenced to E_{pzc} (see main text) determined in the blank curve in panel A. Red and black traces: after ~1h and overnight evacuation of THF at 80°C, respectively. Scan rate of 0.020V s⁻¹.

The potential scale in Fig. 1 has been referenced to the effective *point-of-zero-charge* (E_{pzc}) taken to be the potential central between the limits of the polarizable potential window (PPW) in curve A. The PPW at the w|P₆₆₆₁₄NTf₂ interface is too small to accurately assess the formal ion transfer potentials of multiple ions to conform to the TATB (tetraphenylarsonium-tetraphenylborate) non-thermodynamic assumption which is common convention. Therefore, E_{pzc} was chosen arbitrarily and for convenience so that reference potentials were consistent within this work. The PPW is limited by the supporting electrolyte. In this case, using common conventions for ion transfer (IT) currents [56], either Li⁺ transfers from w→IL or NTf₂⁻ from IL→w, at positive potentials, while either SO₄²⁻, from w→IL, or P₆₆₆₁₄⁺, from IL→w transfers at the negative end. However, the formal Li⁺ transfer potential, $\Delta_{IL}^w \phi_{Li^+}^{o'}$, is probably well

beyond the positive limit [57, 58], and since P_{66614}^+ is quite hydrophobic [59], the PPW is predominately limited by NTf_2^- and SO_4^{2-} transfer (see inset in Fig. 1A). The PPW is 400mV wide and in good agreement with previous results [60-62], but is small compared to ILs incorporating fluorinated phenyl borate anions [18, 56, 58, 63, 64]. The lower viscosity of $P_{66614}NTf_2$, however, makes it easier to manipulate at ambient temperature ($\sim 330\text{mPa s}$, [65, 66]) versus more hydrophobic ILs [18, 54, 56, 58, 63, 64]. Panels B and C show the CVs obtained with a final concentration of 20 and 600mM $LiBH_4$ in the IL. The red and black traces (Panel C) show the system after $\sim 1\text{h}$ and overnight high vacuum evacuation of THF at 80°C , respectively. The negative current offset ($i_{\text{offset}} \sim -0.5\text{nA}$) in the black curve in (C) maybe the result of the continuous transfer of soluble Li^+ since, Li^+ transferring from $IL \rightarrow w$ is negative. Similarly, the red trace in panel C is dominated by a peak-shaped wave ($i_p \sim -1\text{nA}$) at negative potentials (indicated) that limits the PPW reducing it to $\sim 200\text{mV}$ wide. This is likely the transfer of BH_4^- . The amount of soluble $LiBH_4$ was estimated from both curve features, i_{offset} and i_p , using eq. S1 (see SI) to be 5 and 10mM, respectively, much lower than the expected 600mM. The former likely represents the limit of solubility for $LiBH_4$ in $P_{66614}NTf_2$ at low molecular solvent concentrations. The latter is a gross estimate since the entirety of the wave is not visible; therefore, the actual $[LiBH_4]$ is likely much higher. However, when the molecular solvent has been completely removed (overnight) Li^+ and BH_4^- transfers are cancelled suggesting $LiBH_4$ becomes insoluble. This agrees well with a recent study that showed low solubility for a variety of inorganic salts in ILs incorporating P_{66614}^+ [9].

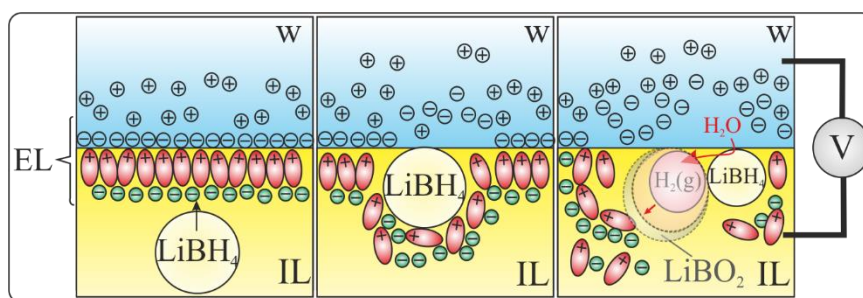
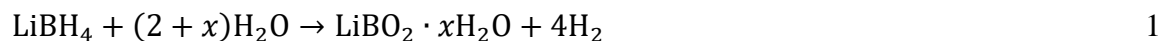


Figure 2: Proposed mechanism of NC adsorption at a w|IL interface with disruption of the back-to-back electric layers (ELs) eliciting a change in the capacitive current. Upon $LiBH_4$ NC impact, an H_2 bubble grows at the NC-w|IL interface with a layer of $LiBO_2$ at the bubble frontier.

Meanwhile, for the $LiBH_4$ added black traces (B,C), negative current spikes, or oscillations, are observed towards negative potentials. Voltammetric current oscillations have been observed previously at w|o LLs by Kakiuchi *et al.* [67-69] and others [70-72]. They were

attributed to the adsorption of ionic surfactants at w|o LLI leading to rapid fluctuations in the IT wave current signal near the species formal IT potential. A thermodynamic model suggested that negative currents would correspond to the adsorption of negatively charged species and vice versa for positively charged ones. In the present case, current spikes are still present, but no IT wave was observed after THF removal that could be associated with molecular adsorption. Therefore, the current spikes may have another origin as they are reminiscent of those observed for NP impacts at ultramicroelectrodes [21-29] or micro-LLIs [30-34]. Since they are related to the presence of LiBH₄ in the IL, and owing to its partial solubility, we propose that the current spikes observed in Figure 1B,C are related to the presence of LiBH₄ crystals, suspended in P₆₆₆₁₄NTf₂, which collide with the LLI through Brownian motion. Owing to the strong reducing strength of LiBH₄, when reaching the w|o interface, the LiBH₄ crystals are expected to undergo a complex 8-electron borohydride oxidation reaction (BOR) [73]:



BOR is the overall reaction for harvesting H₂ from borohydrides. BOR leads to the generation of LiBO₂ material, which is even less soluble in the IL phase, but which could transfer into the aqueous phase without *a priori* charge transfer across the LLI. However, we propose that the overall reaction **1**, or its consequence, disrupts the organized capacitive back-to-back electric layers, similar to the disruption seen with ionic surfactants [67-72]. Such LLI disruption may originate from the adsorption of LiBH₄ crystals, as schematized in Fig. 2, but the formation of LiBO₂ crystals or the generation of H₂ bubbles at the LLI would function equivalently. Uehara *et al.* [74] recently investigated the interfacial formation of Au NPs at a water|1,2-dichloroethane (w|DCE) interface through the Burst-Shiffrin method. They demonstrated BH₄⁻ transfer, however, they employed a 1mM LiOH (pH 11) aqueous solution to inhibit the spontaneous reaction of BH₄⁻ with water. This is not the case here (pH 5-6 for MilliQ water). Therefore, we hypothesize that LiBH₄ NCs react as they contact or approach the w|P₆₆₆₁₄NTf₂ interface, since the P₆₆₆₁₄NTf₂ is likely water saturated in the vicinity of the interface. This is why neither BH₄⁻ ion nor NC transfer is observed. It is well known that the w|IL interface is well organized and can extend several ionic layers into the IL phase [75-79]; Fig. 2 has been drawn with this in mind. That the current spikes are negative may be owing to the release and adsorption of BH₄⁻ in a similar manner as the adsorption of a negatively charged ionic surfactant as described by Kakiuchi [67-72] (see discussion above). Alternatively, the negative current may be due to enhanced ionic conductivity due to solubilization of the LiBH₄ salt and its constituent ions

occupying vacancies in the IL ionic layers [75-79]. In our proposed mechanism no electrons are exchanged across the LLI, since e^- transfer from IL \rightarrow w would elicit a positive current spike.

To investigate the presence and reactivity of LiBH_4 NCs at interfaces, we engaged different microscopic methods. First, a $10\mu\text{L}$ aliquot of the $\text{LiBH}_4\text{-P}_{66614}\text{NTf}_2$ solution prepared above was added to dry, deoxygenated toluene (1mL) and mixed. A TEM grid was suspended in the solution for $\sim 5\text{min}$, then removed and dried under a flow of Ar. Fig. 3A,B show TEM images taken at two different locations within the sample, where the dark objects are LiBH_4 NCs. These images indicate irregularly shaped NCs with high size polydispersity, ranging from $<10\text{nm}$ to $>150\text{nm}$. A larger number of smaller NCs were observed during TEM imaging. This is thought to be owing to three factors: i) there is simply a lower amount of the large NC aggregates, ii) the larger NCs have difficulty adhering to the grid surface, iii) transfer of the NC-IL mixture to toluene alters the NC morphology. Particles from >50 images were measured along their longest axis and a size distribution profile developed (Fig. S2 in SI) and fit using a Gaussian curve with the peak providing a NC diameter of $\sim 10\text{nm}$. DLS analysis of the IL-NC solution provides a distribution of NCs (not shown) whose hydrodynamic diameter is centered rather at $\sim 160\text{nm}$. Larger particles generally mask smaller particle signals within DLS measurements, thus this result is consistent with the LiBH_4 NCs polydispersity revealed by TEM.

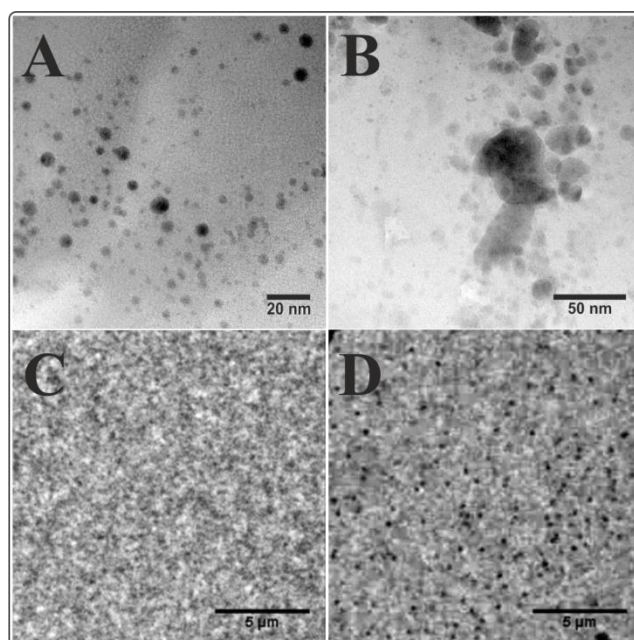


Figure 3: [A-B] TEM images of LiBH_4 NCs. [C-D] Backside absorbing layer optical microscopy (BALM) images taken at $63\times$ magnification in a drop of IL solution containing 0 and 6mM LiBH_4 in $\text{P}_{66614}\text{NTf}_2$, respectively.

Further insight into the presence and reactivity of NCs at interfaces was obtained from optical microscopies, which were performed *in situ* in real time at the interface between a Au layer and the IL phase. This is provided by the BALM technique (see SI Fig. S3), which is based on an ultrathin and highly absorbing gold layer deposited on a glass slide, mounted on an inverted microscope and lit from the bottom. The ~5nm thick Au layer acts as a pseudo-anti-reflective coating and allows imaging of nano-objects lying on its surface with high sensitivity. A nano-object lying on the surface disturbs the local refractive index and therefore the local reflectance at the nano-object-Au layer interface, appearing highly contrasted. BALM was then used to image the presence of LiBH₄ NCs in P₆₆₆₁₄NTf₂. Two drops (5μL each) of the LiBH₄-in-P₆₆₆₁₄NTf₂ solutions were deposited on a BALM substrate. The first contained no LiBH₄ (blank, Fig. 3C) and appears uncontrasted, as the solution does not contain NCs. After deposition of the LiBH₄-IL solution, the image reveals the presence of dark spots, as shown in Fig. 3D. It was also noted that increasing [LiBH₄] causes a concomitant increase in the number of spots. These black optical spots, often diffraction limited, indicate a local decrease in reflectance, which is due to local refractive index increase associated with the presence of a dielectric material at the Au-IL interface. We assume they manifest the presence of LiBH₄ NCs or their reaction product, LiBO₂, through **1** with residual water. ILs are known to be hygroscopic and will absorb moisture from the air, feeding **1**.

The reactivity of the LiBH₄ NCs was probed by BALM. Indeed, micro- or nano-bubbles are also visible in BALM as the technique is sensitive to all local refractive index changes (1.0 and 1.4 for H₂ and the IL, respectively). Therefore, H₂ bubbles at the Au-IL interface appear as more reflective (brighter) regions.

Fig. 4 presents a sequence of BALM images monitoring the formation of two bubbles (indicated by arrows) at the Au surface. These are characterized by the bright spots with radii in the range of 0.3-0.7μm. They last for several tens of seconds (experimentally from t=0 to t=48.35s for the first one) near the Au surface and move slowly (less than 1μm), likely because of the high IL viscosity and also because they are trapped at the Au-IL interface. Even though H₂ is poorly soluble in ILs, the long persistence of the bubbles at the surface suggests that they are anchored to a LiBH₄ NC, which continuously fuels H₂ bubble growth. It is also indicative of the slow transformation rate of the LiBH₄ NC, while we have not attempted to control the H₂O content of the IL. The dynamics of bubble disappearance was also tracked during such movies (at 20fps). This disappearance stems from ending of LiBH₄ reaction with H₂O and corresponds to the H₂ bubble dissolution into the IL solution or the bubble being liberated from

the Au surface. This is simultaneous with the quick ($<0.8\text{s}$ from $t=48.35\text{s}$) expansion of a dark region on the Au surface of a dielectric material. The larger the bubble, the larger the dark region will be. Based on these observations, we suggest that this region is related to the release/deposition of metaborate, LiBO_2 , which is generated during H_2 evolution at the bubble-IL interface and released as a phase transfer process to the more hydrophilic Au region at reaction completion. From a LiBO_2 disc (assuming a thickness of 0.5nm), one can calculate the radius for the originating LiBH_4 NC, such that discs with $r_{\text{disc}}=0.5\text{-}1.0\mu\text{m}$ would develop from NCs with a radius $r_{\text{NC}}=80\text{-}120\text{nm}$, which is in fair agreement with the NC sizes observed microscopically.

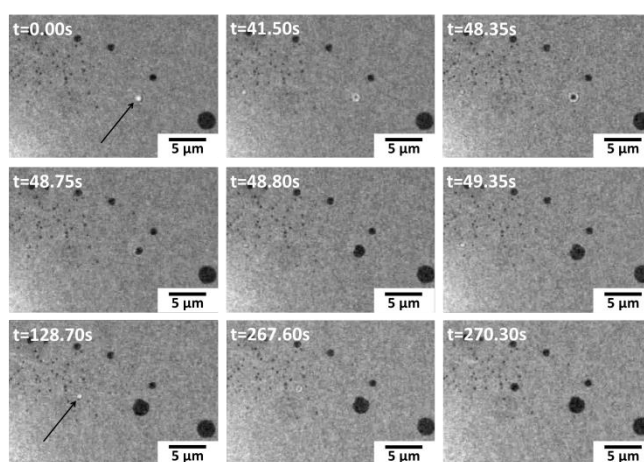


Figure 4: Sequence of BALM images showing two Bubbles (highlighted by arrows) impacting the antireflective substrate. Images were taken in a drop of IL solution containing 6mM LiBH_4 .

LiBH_4 NCs in $\text{P}_{66614}\text{NTf}_2$ were also imaged by darkfield optical microscopy (see SI Fig. S4). Several scattering features are detected in the IL solutions, and their content increases gradually with LiBH_4 content of the solution. However, these scattering spots cannot be unambiguously differentiated from LiBH_4 NCs, as frequently imaged above through TEM, or H_2 bubbles formed in the IL during the reaction between NCs and water molecules. Using the DLS determined diameter as a guide, the NC concentration, c_{NC} , was calculated through Eq. S3 [19, 20] (see SI) assuming spherical particles. For example, c_{NC} for 160nm O particles were calculated to be 3×10^{14} and $8 \times 10^{15} \text{NC L}^{-1}$, for the overall effective $[\text{LiBH}_4]_{\text{eff}}$ (sequestered as NCs + solubilized) of 20 , and 600mM , respectively. This likely underestimates c_{NC} , as the DLS cannot accurately detect the small NCs observed by TEM.

These microscopic observations support, at least semi-quantitatively, the existence of LiBH₄ NCs and their reactivity in an IL toward H₂ generation, as suggested by **1**. They also suggest that this reaction may occur at interfaces.

As the reaction is driven by H₂O, we tested this mechanism at a w|IL interface, via electrochemical monitoring of currents passing through this interface. For that purpose, chronoamperometric (CA) curves were recorded at a micro-LLI at different [LiBH₄]_{eff}. Fig. 5A and inset (a) show CA traces obtained by biasing the potential in Cell 1 at ($E_{pzc} - 0.050V$) without LiBH₄ (blank). In the presence of LiBH₄ NCs, panels B-D for 10, 20, 50mM [LiBH₄]_{eff}, respectively, current spikes are observed to increase in frequency with increasing [LiBH₄]_{eff}. The spike profile is reminiscent of other nano-object impact recordings [19, 20]: a baseline current before, with a sudden onset current (spike) upon NP impact, followed by a decay period (deactivation). Peak durations (obtained from *full-width-at-half-maximum* curve fitting of the spike profile) averaged 0.09s with a maximum of 1.8-2s. Similar results were observed when Li₂SO₄ (aq) was replaced with 5mM H₂SO₄.

Owing to the observation of NCs and H₂ bubble generation in the IL, it is likely that as LiBH₄ NCs in the IL phase contact the aqueous phase they undergo a similar reaction to that observed using BALM – *i.e.* **1**. As proposed earlier (*vide supra*), the adsorption of either crystal phase or the generation of H₂ bubbles at the interface may alter the interfacial double layer, resulting in the observed current spike. It is proposed that the amount of charge displaced by these objects (Q_c) at the interface is proportional to the volume of the LiBH₄ NC impacting it (assuming a sphere with radius r_{NC}) [19, 28, 29]:

$$Q_c \propto \frac{\frac{4}{3}\pi r_{NC}^3 z \rho F}{M_w} \quad [2]$$

where z and F are the charge and Faraday constant, while M_w and ρ are the molecular weight and density of LiBH₄. The current transient, J_c , corresponds to the charge variation during the NC adsorption ($J_c = dQ_c/dt$). From the integration of each baseline corrected current spike an apparent value of r_{NC} was evaluated assuming $z \approx 1$. Fig. 5E shows the histogram obtained for r_{NC} compiled across all [LiBH₄]_{eff} with a Gaussian curve fitting (red trace) centered at 40nm. A mean r_{NC} of 60nm was also determined from these data. Fig. S5 (SI) shows histograms of r_{NC} for each concentration and demonstrates that with increased [LiBH₄]_{eff} there is an increase in the number of large (>100nm \varnothing) NC aggregates. It is possible however, that not all of the particle necessarily interacts with the LLI and partial dissolution/reaction through **1** of the NC may

result. This combined with the high size polydispersity of the NCs explains the variability in current spike size. Furthermore, the associated baseline current noise is $\sim 7\text{-}8\text{pA}$ (Fig. 5A inset (a)), which corresponds to an $r_{\text{NC}} \sim 15\text{-}18\text{nm}$ and represents the effective detection limit of the potentiostat employed.

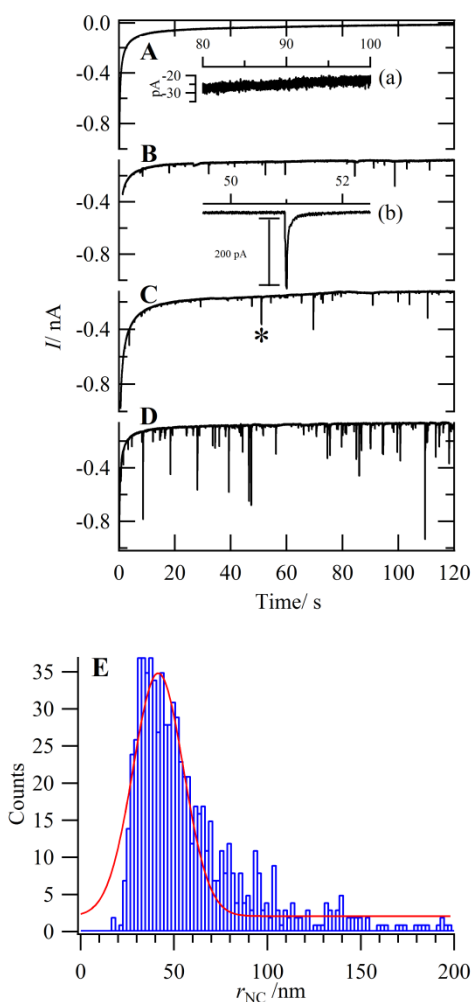


Figure 5: Chronoamperograms (CA) performed at ($E_{\text{pzc}} = -0.050\text{V}$) using Cell 1 with 0, 10, 20, and 50mM $[\text{LiBH}_4]_{\text{eff}}$ for panels **A-D**, respectively. Insets (a) and (b) show enhanced views of curve A and a peak in curve C marked with an (*), respectively. **E** Histogram of r_{NC} calculated from Eq. 2 and by peak integration from the recorded CAs.

The peak signals here resemble more closely single NP impact events than CAs recorded for ionic surfactant adsorption [67-72]. The latter generates truly chaotic recordings, while what is observed here resemble discreet events.

The flux (f) of NC impacts can be calculated through [19, 28]:

$$f = 4D_{\text{NC}}c_{\text{NC}}a \quad [3]$$

where D_{NC} and c_{NC} are the diffusion coefficient and concentration of NC in P₆₆₆₁₄NTf₂, while a is the radius of the LLI (12.5 μm). $D_{\text{NC}} \approx 0.3 \mu\text{m}^2 \text{s}^{-1}$ was calculated via the Stokes-Einstein equation for an $r_{\text{NC}} = 60 \text{nm}$ (used as a first approximation), c_{NC} was calculated to be 3.6, 7.2, and $18.1 \times 10^{11} \text{NC cm}^{-3}$ for Fig. 5 panels B-D, respectively. This leads to a calculated frequency of impacts, f , of 0.2, 0.5, and 1.0s^{-1} compared to the observed values of 0.2, 0.5, and 0.6s^{-1} . These are in fair agreement and support the size polydispersity evidenced using TEM and optics. Moreover, owing the NC reactivity their size is likely not static. Again, for comparison the frequency of H₂ bubble adhesion (or dark spot formation) at the $25 \times 20 \mu\text{m}^2$ Au-IL BALM monitored interface is about 0.015s^{-1} for $6 \text{mM} [\text{LiBH}_4]_{\text{eff}}$, which would indicate that both interfacial phenomena are driven by the same limiting transport of LiBH₄ NCs toward an interface.

CAs (SI, Fig. S6) were performed using Cell 1 with $5 \text{mM Li}_2\text{SO}_4$ (aq) and $600 \text{mM} [\text{LiBH}_4]_{\text{eff}}$ (P₆₆₆₁₄NTf₂), but with potentials stepped from E_{pzc} to $(E_{\text{pzc}} - 0.2 \text{V})$ or $(E_{\text{pzc}} + 0.2 \text{V})$. For the former, an impact was recorded at $f \geq 1 \text{s}^{-1}$, while for the latter it was at $f \approx 0.02 \text{s}^{-1}$. This demonstrates a potential dependence on the impact frequency, which may be related to the IT/adsorption of BH₄⁻ through release from the NC, similar to ionic surfactants [67-72], or the NC zeta-potential. A zeta-potential of 34mV was determined for the NCs in P₆₆₆₁₄NTf₂ from the DLS, but a great deal of error was associated with this measurement ($\pm 0.250 \text{V}$), which should be considered a gross estimate. It may, however, explain the change in f with potential since negatively charged particles would be attracted by the positively biased LLI.

Finally, **1** suggests the generation of H₂ upon LiBH₄-NC approach to the w|IL interface and micrometric H₂ bubbles are indeed generated at a Au/IL interface, as optically recorded (*vide supra*). To investigate this at the LLI we optically monitored, under darkfield illumination, the micro-LLI made by a pulled glass pipette containing the aqueous phase inserted into a home-made cell (SI, Fig. S7) containing the IL phase. Fig. 6A shows a still image at $40\times$ magnification captured from a video taken at the pipette tip (inner tip diameter $\sim 50 \mu\text{m}$), housing the aqueous phase with $5 \text{mM Li}_2\text{SO}_4$, immersed in a $20 \text{mM} [\text{LiBH}_4]_{\text{eff}}$ P₆₆₆₁₄NTf₂ solution. A layer of effervescence can be seen at the pipette tip, which developed immediately upon immersion of the pipette into the IL phase, and is likely the formation of H₂ bubbles according to **1**. This means that monitoring the w|IL interface is not possible. Bubbles were observed to rise from the tip and accumulate on the upper glass-slide surface (SI, Fig. S7); however, this process was slow and consistent with the long bubble residency-time on the Au-IL interface. The layer of H₂

bubbles at the w|IL interface would lead to Marangoni-like effects, which are described as changes in surface tension at liquid-air or liquid|liquid interfaces [80] that in turn cause increased hydrodynamic flow, much faster than diffusion alone. Indeed, this may be used to explain the increased number of larger current spikes (magnitude > 0.4 nA) observed at 50 mM vs. 20 or 10 mM $[\text{LiBH}_4]_{\text{eff}}$ in Fig. 5B-D. With increased hydrodynamic flux larger NCs have increased mobility and are more readily detected at the LLI.

Similarly, it is proposed that the disparity between the calculated and observed flux of NCs at $\sim E_{\text{pzc}}$ is owing to two factors: (i) the gross estimate of [NC] due to their polydispersity; (ii) an enhancement of the flux through H_2 -in-IL foam formation causing Marangoni-like effects.

Fig. 6B provides a close-up of the pipette tip and H_2 foam. The red line (arrow) describes the location from which a plot profile (inset) of the local scattered light intensity, I_{opt} , was taken, with the x-coordinate corresponding to the red line length scale. This details the diameter of the bright-spot, $\sim 1 \mu\text{m}$, and is consistent with the size of the H_2 bubbles detected at the Au/IL interface. It also corroborates H_2 bubble formation close to the w|IL interface. The effervescent region corresponds to a dense region of bubbles. It first suggests that H_2 is preferentially generated in the IL phase, a diffuse region of bubbles is indicative of the partial solubility of H_2O in the IL. Over several tens of seconds this diffuse layer of H_2 bubbles has a steady size, supporting the long persistence of H_2 bubbles also monitored, at the single bubble level, at the Au-IL interface. Because the pipette was mounted horizontally (SI, Fig. S7), the bubbles were observed to detach slowly from the LLI, rise and accumulate at the top of the cell. Using a mass-transfer limited H_2 dissolution rate analogous to Eq. 3 as a *back-of-the-envelope* calculation, with $D_{\text{H}_2(g)}$ and $c_{\text{H}_2\text{sat/d}}$ (saturated $[\text{H}_2]$) of $10^{-6} \text{cm}^2 \text{s}^{-1}$ and $\sim 2 \text{mM}$ [81-83], along with $a=25 \mu\text{m}$, one estimates a rate of H_2 evolution at 0.02pmol s^{-1} . Considering the full foam region, Comsol simulation (SI section 10) rather gives a rate of 0.04pmol s^{-1} of H_2 generated (semispherical diffusion regime) from this LLI interface, yielding a flux of $1.6 \text{nmol cm}^{-2} \text{s}^{-1}$.

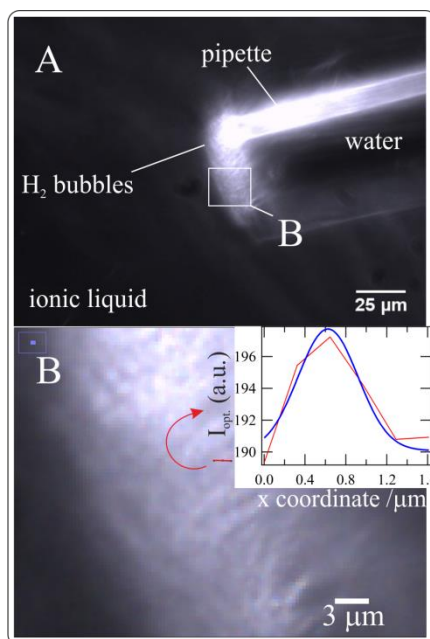


Figure 6: **A** is a darkfield optical image of a pulled glass pipette tip containing a 5mM Li_2SO_4 aqueous solution immersed in $\text{P}_{66614}\text{NTf}_2$ containing 20mM $[\text{LiBH}_4]_{\text{eff}}$. **B** shows a close-up image taken from **A** (indicated) of the H_2 gas-in-IL foam field. Inset in **B**: local scattering light intensity, $I_{\text{opt.}}$, vs. an x -coordinate defined by the red line in **B** and describing a single H_2 bubble; fit using a Gaussian function (blue trace).

Similarly, Eq. 2 can be taken from the perspective of the charge displaced on either side of the w|IL interface as related to their respective Debye lengths, coupled to an effective surface area affected ($A \approx 4\pi r^2$, using a sphere as a first approximation) and the current spike integral, see SI section 11 for calculation details. In this way, the effected ‘radius’ was calculated to be $\sim 1\text{-}2\mu\text{m}$ regardless of whether it was the IL or w side of the interface. This agrees well with the size of H_2 bubbles recorded in Fig. 6.

It is then suggested that solutions of LiBH_4 in $\text{P}_{66614}\text{NTf}_2$ can be used to deliver H_2 at reasonable rates; similar results are expected for LiBH_4 in P_{888}Br , an organic ionic plastic crystal (OIPC) [18]. In a typical GC column experiment, 0.4mL aliquots of 600mM $[\text{LiBH}_4]_{\text{eff}}$ in $\text{P}_{66614}\text{NTf}_2$ were placed into each of 5 sealed GC vials with the IL and headspace gases maintained under Ar. Next, 1 μL of degassed H_2O was added to the vials. The headspace of one of the 5 vials was sampled every $\sim 10\text{min}$ using a 250 μL air-tight syringe and injected into a GC column in order to develop a profile of $\Delta[\text{H}_2]/t$. This protocol was repeated for the other materials (LiBH_4 in P_{888}Br , $\text{LiBH}_4 + \text{Au-NPs}$ in P_{888}Br , *etc.*). A plot of $[\text{H}_2]$ in the headspace over time is given in Fig. 7 for the IL and OIPC media with only LiBH_4 (600mM) alone or in the

presence of Au or Pt NPs (see SI Fig. S10 for TEM images of the as-prepared NPs). Based on the results from Fig. 7, the presence of metal NPs within the IL or OIPC phase had little effect on H₂ evolution. This is likely owing to the low diffusion coefficient (mass transport) of H₂O and NPs in the IL reducing the observed reaction rate. After 10 and 20min, 20 and 50%, respectively, of the theoretical H₂ has been liberated. This is slow compared to, for example, NaBH₄ dissolved in water in combination with certain accelerators, as demonstrated by Schlensinger *et al.* [84]. This does demonstrate, however, that the IL and OIPC media can be support phases for LiBH₄/H₂ storage, but reaction rates are likely limited by their relatively high viscosity (diffusivity and solubility of H₂ within these matrices) compared to molecular solvents. During sampling the OIPC was a solid/plastic and hence this indicates possible increased activity of the OIPC film vs. the IL, since in the former, the H₂O droplet rests on the solids surface while in the latter the droplet is fully immersed in the liquid phase. This would result in less surface contact for the OIPC case, but more needs to be done to investigate this point; this is beyond the scope the present work.

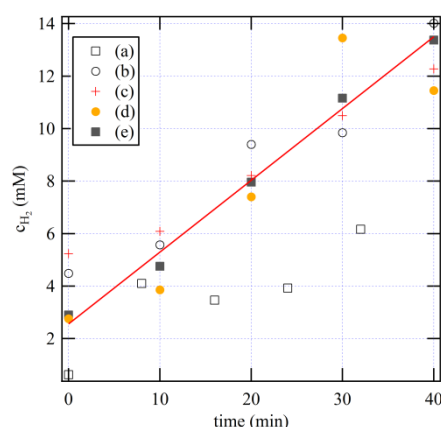


Figure 7: Plot of the concentration of H₂ (mM) evolved in the headspace of a GC vial containing either P₆₆₆₁₄NTf₂, an ionic liquid (IL), or P₈₈₈₈Br, an organic ionic plastic crystal (OIPC) over time (min), with (a) 600mM of [LiBH₄]_{eff} in IL, (b) a + Au NPs, (c) 600mM LiBH₄ in OIPC, (d) c + Au NPs, and (e) a + Pt NPs. TEM images of NPs are shown in Fig. S10 (SI).

For comparison purposes, the flux of H₂ generated by the pipette was extrapolated to that of the surface area of the 1μL water droplet deposited in the vial (r≈620μm) for the GC experiment. The GC rate was further corrected, based on the difference in LiBH₄ concentration (20 vs. 600mM, *i.e.* factor 30) between the pipette and GC experiments. From the pipette flux of H₂, one expects a rate of 0.1nmol s⁻¹ H₂, while during the GC experiment 0.2nmol s⁻¹ in the headspace was observed. These values are in good agreement.

4.0 Conclusions

The convergence of multiple techniques, ranging from *ex situ* TEM to *in situ* high-resolution optical microscopies and electrochemical stochastic impacts experiments at a w|IL interface, evidence the formation and reactivity of LiBH₄ NCs in an IL medium. TEM measurements are not ideal, since transfer of the IL-inorganic salt solution to a molecular solvent, in order to facilitate sample deposition on the TEM grid, undoubtedly alters the NC morphology. At the same time, the TEM beam can be destructive to certain samples and thus may not be innocent either. Thus, the use of high-resolution microscopies, such as BALM and darkfield, were integral in establishing the presence and reactivity of LiBH₄ NCs suspended in an IL, particularly at different interfaces (Au/IL and w|IL). The solubility of inorganic salts in ILs is an emerging field of study, especially with ILs and OIPCs being proposed liquid/solid electrolyte phases for lithium ion batteries. As highlighted with this work, this is another critical physical chemical property of ILs that will have to be tailored to meet specific application needs.

An attempt has been made herein to extend electrochemical nano-impact studies beyond model systems (e.g. metal NPs or insulating polymer NPs). In the present case, the proposed mechanism is based on charge displacement or adsorption altering the *back-to-back* electric layers during NC impact, which in turn creates a change in the interfacial capacitance. This agrees well with the adsorption of charged species, such as ionic surfactants, as demonstrated in the past. The frequency of impacts was in relatively good agreement with the calculated value considering the high polydispersity of the NCs and Marangoni effects through H₂-in-IL micro/nano foams, which generates an increased hydrodynamic flow.

Critically, the formation of H₂-in-IL foams represents a possible facile method for the generation of H₂ bubbles in an IL phase whose nucleation is of interest in heterogeneous catalyst design [85-87] and should be of particular significance for LLI solar fuel generation (*i.e.* H₂ or O₂ evolution/reduction reactions) moving forward.

Acknowledgements

We are grateful for financial support by the Agence Nationale pour la Recherche (NEOCASTIP-ANR-15-CE09-0015-02). T.J.S. would like to gratefully acknowledge funding through a Marie-Sklodowska Curie Action incoming post-doctoral fellowship (MSCA-IF, project #DLV-708814). Partial financial support to M. R. from the Institut Universitaire de France (IUF) is gratefully thanked. T.J.S would also like to thank Pr. Alexa Courty and Dr. Guillaume Wang for help in TEM imaging.

5.0 References

- [1] M. Paskevicius, L.H. Jepsen, P. Schouwink, R. Cerny, D.B. Ravnsbaek, Y. Filinchuk, M. Dornheim, F. Besenbacher, T.R. Jensen, *Chem. Soc. Rev.*, 46 (2017) 1565-1634.
- [2] H.-W. Li, Y. Yan, S.-i. Orimo, A. Züttel, C.M. Jensen, *Energies*, 4 (2011) 185.
- [3] A. Doroodian, J.E. Dengler, A. Genest, N. Rösch, B. Rieger, *Angew. Chem. Int. Ed.*, 49 (2010) 1871-1873.
- [4] R. Mohtadi, A. Remhof, P. Jena, *J. Phys.: Condens. Matter*, 28 (2016) 353001/353001-353001/353019.
- [5] J. Ma, N.A. Choudhury, Y. Sahai, *Renew. Sust. Energy Rev.*, 14 (2010) 183-199.
- [6] S.C. Amendola, P. Onnerud, M.T. Kelly, P.J. Petillo, S.L. Sharp-Goldman, M. Binder, *J. Power Sources*, 84 (1999) 130-133.
- [7] S. Wegner, C. Janiak, *Top. Curr. Chem.*, 375 (2017) 1-32.
- [8] G. Durga, A. Mishra, *Ionic Liquids: Industrial Applications*, in: *Encyclopedia of Inorganic and Bioinorganic Chemistry*, John Wiley & Sons, Ltd, 2011.
- [9] A.B. Pereiro, J.M.M. Araújo, F.S. Oliveira, J.M.S.S. Esperança, J.N. Canongia Lopes, I.M. Marrucho, L.P.N. Rebelo, *J. Chem. Thermodyn.*, 55 (2012) 29-36.
- [10] C. Janiak, *Top. Organomet. Chem.*, 51 (2015) 17-53.
- [11] J.D. Scholten, B.C. Leal, J. Dupont, *ACS Catalysis*, 2 (2010) 184-200.
- [12] A. Banerjee, R.W.J. Scott, Au, Ag, and Cu Nanostructures, in: *Nanocatalysis in Ionic Liquids*, Wiley-VCH, 2016, pp. 97-123.
- [13] A. Banerjee, R. Theron, R.W.J. Scott, *Chem. Commun.*, 49 (2013) 3227-3229.
- [14] A. Banerjee, R.W.J. Scott, *Green Chem.*, 17 (2015) 1597-1604.
- [15] M. Antonietti, D. Kuang, B. Smarsly, Y. Zhou, *Angew. Chem. Int. Ed.*, 43 (2004) 4988-4992.
- [16] X. Chen, S.L. Chew, F.M. Kerton, N. Yan, *Green Chem.*, 16 (2014) 2204-2212.
- [17] T.S. Hansen, J. Mielby, A. Riisager, *Green Chem.*, 13 (2011) 109-114.
- [18] T.J. Stockmann, P.D. Boyle, Z. Ding, *Catal. Today*, 295 (2017) 89-94.
- [19] S.V. Sokolov, S. Eloul, E. Katelhon, C. Batchelor-McAuley, R.G. Compton, *Phys. Chem. Chem. Phys.*, 19 (2017) 28-43.
- [20] P.H. Robbs, N.V. Rees, *Phys. Chem. Chem. Phys.*, 18 (2016) 24812-24819.
- [21] B.M. Quinn, P.G. van't Hof, S.G. Lemay, *J. Am. Chem. Soc.*, 126 (2004) 8360-8361.
- [22] J.E. Dick, C. Renault, A.J. Bard, *J. Am. Chem. Soc.*, 137 (2015) 8376-8379.
- [23] X. Xiao, A.J. Bard, *J. Am. Chem. Soc.*, 129 (2007) 9610-9612.
- [24] B.-K. Kim, J. Kim, A.J. Bard, *J. Am. Chem. Soc.*, 137 (2015) 2343-2349.
- [25] H.S. Toh, R.G. Compton, *Chem. Sci.*, 6 (2015) 5053-5058.
- [26] E.E.L. Tanner, K. Tschulik, R. Tahany, K. Jurkschat, C. Batchelor-McAuley, R.G. Compton, *J. Phys. Chem. C*, 119 (2015) 18808-18815.
- [27] A. Feng, W. Cheng, R.G. Compton, *Chem. Sci.*, 7 (2016) 6458-6462.
- [28] V. Brasiliense, A.N. Patel, A. Martinez-Marrades, J. Shi, Y. Chen, C. Combellas, G. Tessier, F. Kanoufi, *J. Am. Chem. Soc.*, 138 (2016) 3478-3483.
- [29] E. Kätelhön, E.E.L. Tanner, C. Batchelor-McAuley, R.G. Compton, *Electrochim. Acta*, 199 (2016) 297-304.
- [30] E. Laborda, A. Molina, V.F. Espín, F. Martínez-Ortiz, J. García de la Torre, R.G. Compton, *Angew. Chem. Int. Ed.*, 56 (2017) 782-785.
- [31] T.J. Stockmann, L. Angelé, V. Brasiliense, C. Combellas, F. Kanoufi, *Angew. Chem. Int. Ed.*, 56 (2017) 13493-13497.
- [32] D.A. Robinson, A.M. Kondajji, A.D. Castañeda, R. Dasari, R.M. Crooks, K.J. Stevenson, *J. Phys. Chem. Lett.*, 7 (2016) 2512-2517.

- [33] R. Dasari, D.A. Robinson, K.J. Stevenson, *J. Am. Chem. Soc.*, 135 (2013) 570-573.
- [34] T.R. Bartlett, C. Batchelor-McAuley, K. Tschulik, K. Jurkschat, R.G. Compton, *ChemElectroChem*, 2 (2015) 522-528.
- [35] M. Heyrovsky, J. Jirkovsky, M. Struplova-Bartackova, *Langmuir*, 11 (1995) 4300-4308.
- [36] M. Heyrovsky, J. Jirkovsky, M. Struplova-Bartackova, *Langmuir*, 11 (1995) 4309-4312.
- [37] M. Heyrovsky, J. Jirkovsky, B.R. Mueller, *Langmuir*, 11 (1995) 4293-4299.
- [38] M. Heyrovsky, J. Jirkovsky, *Langmuir*, 11 (1995) 4288-4292.
- [39] H. Deng, J.E. Dick, S. Kummer, U. Kragl, S.H. Strauss, A.J. Bard, *Anal. Chem.*, 88 (2016) 7754-7761.
- [40] B.-K. Kim, A. Boika, J. Kim, J.E. Dick, A.J. Bard, *J. Am. Chem. Soc.*, 136 (2014) 4849-4852.
- [41] W. Cheng, R.G. Compton, *Angew. Chem. Int. Ed.*, 54 (2015) 7082-7085.
- [42] J.-F. Lemineur, J.-M. Noël, C. Combellas, D. Ausserré, F. Kanoufi, *Faraday Discuss.*, (2018).
- [43] J.-F. Lemineur, J.-M. Noël, D. Ausserré, C. Combellas, F. Kanoufi, *Angew. Chem. Int. Ed.*, 57 (2018) 11998-12002.
- [44] V. Brasiliense, J. Clausmeyer, P. Berto, G. Tessier, C. Combellas, W. Schuhmann, F. Kanoufi, *Anal. Chem.*, 90 (2018) 7341-7348.
- [45] C. Schopf, A. Wahl, A. Martín, A. O'Riordan, D. Iacopino, *J. Phys. Chem. C*, 120 (2016) 19295-19301.
- [46] L. Xiao, Y. Qiao, Y. He, E.S. Yeung, *Anal. Chem.*, 82 (2010) 5268-5274.
- [47] A.N. Patel, A. Martinez-Marrades, V. Brasiliense, D. Koshelev, M. Besbes, R. Kuszelewicz, C. Combellas, G. Tessier, F. Kanoufi, *Nano Lett.*, 15 (2015) 6454-6463.
- [48] X. Li, L. Ren, J. Dunevall, D. Ye, H.S. White, M.A. Edwards, A.G. Ewing, *ACS Nano*, 12 (2018) 3010-3019.
- [49] V. Brasiliense, J. Clausmeyer, A.L. Dauphin, J.-M. Noël, P. Berto, G. Tessier, W. Schuhmann, F. Kanoufi, *Angew. Chem. Int. Ed.*, (2017) n/a-n/a.
- [50] R. Hao, Y. Fan, B. Zhang, *J. Am. Chem. Soc.*, 139 (2017) 12274-12282.
- [51] Y. Yu, V. Sundaresan, S. Bandyopadhyay, Y. Zhang, M.A. Edwards, K. McKelvey, H.S. White, K.A. Willets, *ACS Nano*, 11 (2017) 10529-10538.
- [52] X. Shan, I. Díez-Pérez, L. Wang, P. Wiktor, Y. Gu, L. Zhang, W. Wang, J. Lu, S. Wang, Q. Gong, J. Li, N. Tao, *Nature Nanotechnology*, 7 (2012) 668.
- [53] C.J. Bradaric, A. Downard, C. Kennedy, A.J. Robertson, Y. Zhou, *Green Chem.*, 5 (2003) 143-152.
- [54] T.J. Stockmann, Y. Lu, J. Zhang, H.H. Girault, Z. Ding, *Chem. Eur. J.*, 17 (2011) 13206-13216.
- [55] T.J. Stockmann, A.-M. Montgomery, Z. Ding, *Can. J. Chem.*, 90 (2012) 836-842.
- [56] Z. Samec, J. Langmaier, T. Kakiuchi, *Pure Appl. Chem.*, 81 (2009) 1473-1488.
- [57] T.J. Stockmann, Z. Ding, *Phys. Chem. Chem. Phys.*, 14 (2012) 13949-13954.
- [58] T.J. Stockmann, Z. Ding, *J. Phys. Chem. B*, 116 (2012) 12826-12834.
- [59] T.J. Stockmann, R. Guterman, P.J. Ragona, Z. Ding, *Langmuir*, 32 (2016) 12966-12974.
- [60] N. Tsujioka, S. Imakura, N. Nishi, T. Kakiuchi, *Anal. Sci.*, 22 (2006) 667-671.
- [61] B.M. Quinn, Z. Ding, R. Moulton, A.J. Bard, *Langmuir*, 18 (2002) 1734-1742.
- [62] T.J. Stockmann, Z. Ding, *J. Electroanal. Chem.*, 649 (2010) 23-31.
- [63] T. Kakiuchi, *Anal. Chem.*, 79 (2007) 6442-6449.
- [64] N. Nishi, H. Murakami, S. Imakura, T. Kakiuchi, *Anal. Chem.*, 78 (2006) 5805-5812.
- [65] R.E. Del Sesto, C. Corley, A. Robertson, J.S. Wilkes, *J. Organomet. Chem.*, 690 (2005) 2536-2542.
- [66] T.J. Stockmann, J. Zhang, J.C. Wren, Z. Ding, *Electrochim. Acta*, 62 (2012) 8-18.
- [67] Y. Kitazumi, T. Kakiuchi, *Langmuir*, 25 (2009) 10829-10833.

- [68] T. Kakiuchi, M. Chiba, N. Sezaki, M. Nakagawa, *Electrochem. Commun.*, 4 (2002) 701-704.
- [69] T. Kakiuchi, *J. Electroanal. Chem.*, 536 (2002) 63-69.
- [70] M. Chowdhury, R. Katakly, *ChemPhysChem*, 17 (2016) 105-111.
- [71] M.A. Méndez, Z. Nazemi, I. Uyanik, Y. Lu, H.H. Girault, *Langmuir*, 27 (2011) 13918-13924.
- [72] M.A. Méndez, B. Su, H.H. Girault, *J. Electroanal. Chem.*, 634 (2009) 82-89.
- [73] M.J.F. Ferreira, L. Gales, V.R. Fernandes, C.M. Rangel, A.M.F.R. Pinto, *Int. J. Hydrogen Energy*, 35 (2010) 9869-9878.
- [74] A. Uehara, S.G. Booth, S.Y. Chang, S.L.M. Schroeder, T. Imai, T. Hashimoto, J.F.W. Mosselmans, R.A.W. Dryfe, *J. Am. Chem. Soc.*, 137 (2015) 15135-15144.
- [75] Y. Yasui, Y. Kitazumi, R. Ishimatsu, N. Nishi, T. Kakiuchi, *J. Phys. Chem. B*, 113 (2009) 3273-3276.
- [76] M.V. Fedorov, A.A. Kornyshev, *Chem. Rev.*, 114 (2014) 2978-3036.
- [77] N. Georgi, A.A. Kornyshev, M.V. Fedorov, *J. Electroanal. Chem.*, 649 (2010) 261-267.
- [78] M.V. Fedorov, N. Georgi, A.A. Kornyshev, *Electrochem. Commun.*, 12 (2010) 296-299.
- [79] d.E.E. Alvarez, S.D. S., A.D.W. M., *Angew. Chem. Int. Ed.*, 54 (2015) 14903-14906.
- [80] S. Berg, *Physics of Fluids*, 21 (2009) 032105.
- [81] Z. Lei, C. Dai, B. Chen, *Chem. Rev.*, 114 (2014) 1289-1326.
- [82] J. Jacquemin, P. Husson, V. Majer, M.F. Costa Gomes, *J. Solution Chem.*, 36 (2007) 967-979.
- [83] D. Morgan, L. Ferguson, P. Scovazzo, *Industrial & Engineering Chemistry Research*, 44 (2005) 4815-4823.
- [84] H.I. Schlesinger, H.C. Brown, A.E. Finholt, J.R. Gilbreath, H.R. Hoekstra, E.K. Hyde, *J. Am. Chem. Soc.*, 75 (1953) 215-219.
- [85] Y. Liu, M.A. Edwards, S.R. German, Q. Chen, H.S. White, *Langmuir*, 33 (2017) 1845-1853.
- [86] Q. Chen, L. Luo, H.S. White, *Langmuir*, 31 (2015) 4573-4581.
- [87] Q. Chen, L. Luo, H. Faraji, S.W. Feldberg, H.S. White, *J. Phys. Chem. Lett.*, 5 (2014) 3539-3544.